JOURNAL OF SOLID STATE CHEMISTRY **129,** 147–156 (1997)
ARTICLE NO. SC967254

A First-Principles Investigation of the Electronic Structure and the Chemical Bonding for $CaFe_2P_2$ and $CaNi_2P_2$

E. Gustenau, P. Herzig, and A. Neckel

Institut für Physikalische Chemie, Universität Wien, Währingerstrasse 42, A-1090 Vienna, Austria

Received July 31, 1996; in revised form December 2, 1996; accepted December 3, 1996

DEDICATED TO PROFESSOR W. JEITSCHKO ON THE OCCASION OF HIS 60TH BIRTHDAY

For tetragonal $CaFe_2P_2$ and $CaNi_2P_2$ with $ThCr_2Si_2$ structure self-consistent full-potential LAPW band-structure calculations have been performed. Both compounds show metallic behavior. Bands predominantly originating from P *s* states are found approximately 0.8 Ry below the Fermi energy. After a gap a ca. 0.5 Ry wide region of overlapping, occupied bands is observed. The bottom part of this band complex is formed by bands originating from P *p* states while in the upper part bands with a high Fe or Ni *d* character, respectively, are dominant. An analysis of the bonding situation in the two compounds is performed in terms of local partial densities of states, partial charges, and electron density plots. The main contributions to covalent bonding are due to Fe–Fe/Ni–Ni, Fe–P/Ni–P, and P–P interactions in the respective compounds, where the latter are considerably stronger in $CaNi_2P_2$ (corresponding to the shorter P–P distances in this compound) while the opposite is true especially for the Ni–Ni bonds (first and second neighbors) as compared to the Fe–Fe bonds in $CaFe_2P_2$. Also nonnegligible covalent Ca–Ca, Ca–Fe/Ca–Ni, and Ca–P interactions are found in both compounds.

INTRODUCTION

Roughly 700 compounds of composition AB_2X_2 crystallize in the $ThCr_2Si_2$ structure (1), where in general A is an alkaline earth or a rare earth element, B a transition metal or a main group element, and X an element from groups 13, 14, or 15 of the periodic table (mainly B, Al, Si, Ge, P, and As). This structure, which is an ordered ternary variety of the $BaAl_4$ ($D1_3$) structure, is also referred to as $CeAl_2Ga_2$ type by some authors, a designation introduced by Zarechnyuk *et al.* (2) in 1964. Many compounds of this type show a variety of extraordinary physical properties, such as valence fluctuations and mixed valency (3) (e.g., for $EuNi_2P_2$), superconductivity (4) ($LaRu_2P_2$, $T_c = 4.1$ K), and a wide range of different magnetic structures (see, e.g., (5, 6)).

Within the $ThCr_2Si_2$ structure type striking differences exist regarding the bonding situation. While in $SrFe_2P_2$, e.g., the shortest P–P distance is 3.43 Å, the corresponding value for $CaFe_2P_2$ is 2.71 Å and only 2.30 Å for $CaNi_2P_2$ (7), which is very close to the experimental value for a P–P single bond. Therefore, and because $CaFe_2P_2$ and $CaNi_2P_2$ show only Pauli paramagnetism (8, 9), these two compounds were selected for a first investigation by means of the Linearized Augmented Plane-Wave (LAPW) method (10, 11), using the full-potential version (FLAPW method (12)).

Previous theoretical investigations of these compounds are scarce, despite their very interesting properties, and are confined to calculations on the basis of the Extended Hückel Method (13–15).

In the first theoretical paper (13) on compounds with $ThCr_2Si_2$ structure, Hoffmann and Zheng started their discussion of the bonding properties of $BaMn_2P_2$ with a two-dimensional $Mn_2P_2^{2-}$ layer. In a next step the effects are analyzed which are observed when the $Mn_2P_2^{2-}$ sublattice is formed from the layers and finally when the Ba^{2+} counterions are inserted into the structure. The fact that the P–P distance is strongly dependent on the composition of the crystal is demonstrated using a rigid-band model. In a further paper (14) the differences in the energetics and the bonding situation for the $ThCr_2Si_2$ and the closely related $CaAl_2Si_2$ structure are discussed. The thermodynamic properties of the compounds with $ThCr_2Si_2$ and $CaBe_2Ge_2$ structures are compared in a recent publication by Zheng (15). The author comes to the conclusion that the former structure is more stable at lower temperatures and the latter structure at higher temperatures.

COMPUTATIONAL DETAILS

For the electronic band-structure calculations the FLAPW method (12) with a Barth–Hedin exchange-correlation potential (16) was used. For the l expansion of the potential and the electron density within the muffin-tin spheres terms up to $l = 8$ were taken into account. For the wave function plane waves in the interstitial region were

0022-4596/97 $25.00

included up to a length of $4(2\pi/a)$. The chosen plane-wave basis corresponds to approximately 600 basis functions. For the self-consistency procedure 45 k points in the irreducible part of the Brillouin zone (BZ) were used which is sufficient for the calculation of electron densities. For the band-structure plots the energy eigenvalues for 381 k points ($CaFe_2P_2$) and 379 k points ($CaNi_2P_2$) were calculated. The BZ integration was performed by means of the linearized tetrahedron method (17).

The tetragonal unit cell for $CaFe_2P_2$ and $CaNi_2P_2$ is shown in Fig. 1 and the input parameters for the FLAPW band structure calculations are given in Table 1. The lattice parameters used for the present calculation are the experimental parameters taken from (7). Local coordinate systems for the different atoms are defined as follows. The z axes are always parallel to the c axis of the unit cell. For Ca and Fe or Ni the x and y axes are chosen such that the $d_{x^2-y^2}$ orbital lobes point toward the nearest neighbors of the same atomic species (see Table 2).

RESULTS

(a) Band Structures and Densities of States

The band structures of the valence bands of $CaFe_2P_2$ and $CaNi_2P_2$ are shown in Fig. 2. Two bands, which appear in the energy region between -0.390 and -0.178 Ry for $CaFe_2P_2$ and -0.418 and -0.166 Ry for $CaNi_2P_2$ (with respect to the average potential in the interstitial region), originating from the P 3s states appear that are denoted as "P s band." The corresponding peaks in the densities of states (DOS; see Fig. 3) are dominated by the P s partial DOS with small contributions from Ca and Fe (Ni) states.

The "P s band" is separated from the other bands at higher energies by a gap of 0.27 Ry (3.6 eV) for $CaFe_2P_2$ and 0.24 Ry (3.3 eV) for $CaNi_2P_2$, respectively.

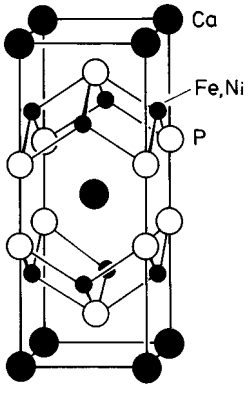

FIG. 1. Tetragonal unit cell for $CaFe_2P_2$ and $CaNi_2P_2$ crystallizing in the $ThCr_2Si_2$ structure.

TABLE 1
Input Parameters for the FLAPW Band-Structure Calculations for $CaFe_2P_2$ and $CaNi_2P_2$ (in a.u.)

Quantity		$CaFe_2P_2$	$CaNi_2P_2$
Lattice parameters	a	7.28489	7.40017
	c	18.86891	17.69350
Muffin-tin sphere radii	R_{Ca}	2.88000	2.88000
	$R_{Fe,Ni}$	1.97892	1.97892
	R_P	1.97892	1.97892

The following six bands are caused by P 3p states ("P p band"). This "band" overlaps with the "Fe/Ni d band," a complex of 10 rather flat bands originating from Fe/Ni 3d states and extending to an energy of about 0.75 Ry which is roughly 0.2 Ry above the Fermi level (0.5574 Ry for $CaFe_2P_2$, 0.5623 Ry for $CaNi_2P_2$).

Figure 3 shows the total DOS and the most important local l-like components, i.e., P s, P p, and Fe or Ni d, respectively, which roughly correspond to the positions of the "bands" defined above. The first double-peak corresponds to P–P s–s σ and σ^* bonds. This can be seen from electron density plots for the two relevant Γ states which are given in Fig. 4. (In Table 3 a charge analysis for these states can be found). After the gap a series of relatively sharp peaks follows. The lower part of this energy region is dominated by P p_z and (p_x, p_y), as well as Fe/Ni d DOS components. Electron densities for two characteristic Γ states (see Fig. 5) show a bonding P–P p_z–p_z state, energetically at the low edge of the energy interval, and an antibonding one at the top. For the peaks in an energy range of ca. 0.3 Ry below the Fermi level the transition metal d character is by far the most important component. This is the region where the states occur which are mainly involved in the formation of bonding and antibonding Fe–P/Ni–P (Fig. 7) and Fe–Fe/Ni–Ni first and second nearest neighbor interactions (Figs. 8 and 9), but also of some weaker bonding interactions, namely P–P (p_x, p_y)–(p_x, p_y) for second nearest neighbors (Fig. 6) and covalent bonds involving the Ca atoms (Ca–Ca $d_{x^2-y^2}$–$d_{x^2-y^2}$ σ, Ca–Fe/Ca–Ni $d_{x^2-y^2}$–d_{z^2} and

TABLE 2
Structural Parameters for $CaFe_2P_2$ and $CaNi_2P_2$ (Space Group *I4/mmm*, No. 139)

		$CaFe_2P_2$			$CaNi_2P_2$		
		x	y	z	x	y	z
Ca	2a	0	0	0	0	0	0
Fe/Ni	4d	0	$\frac{1}{2}$	$\frac{1}{4}$	0	$\frac{1}{2}$	$\frac{1}{4}$
P	4e	0	0	0.3643	0	0	0.3774

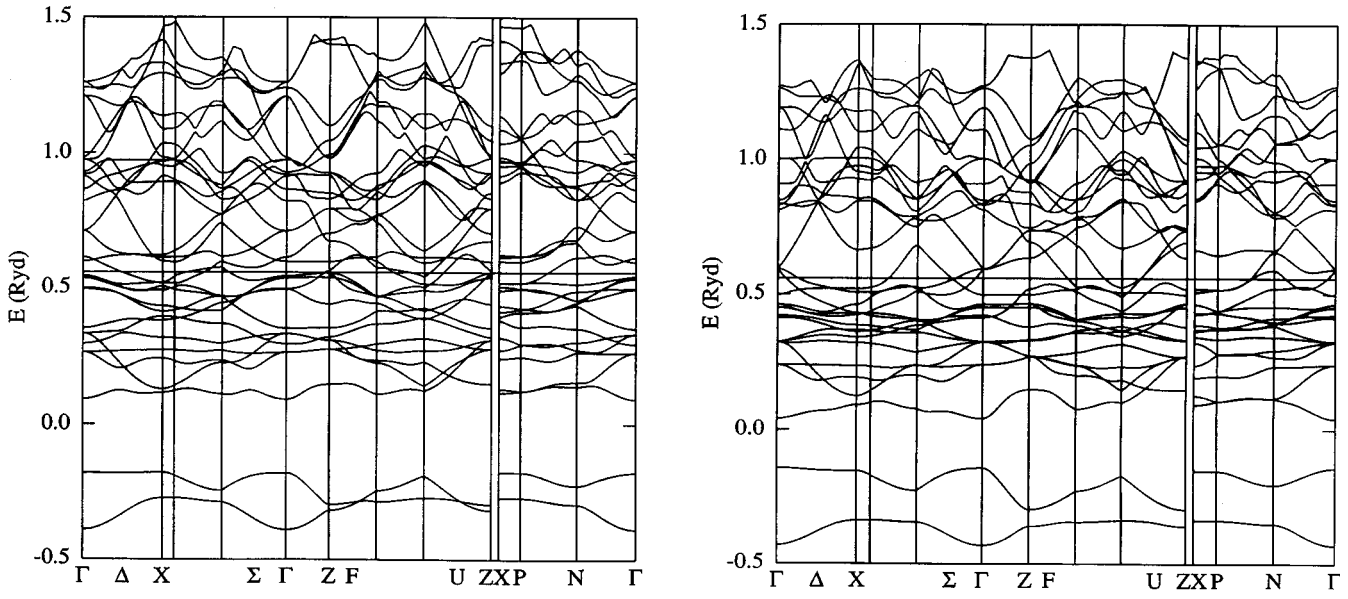

FIG. 2. Band structures of $CaFe_2P_2$ (left) and $CaNi_2P_2$ (right). The energy scale is with respect to the averaged potential in the interstitial region. (The Brillouin zone is the one for the body-centered tetragonal Bravais lattice.)

(d_{xz}, d_{yz})–d_{xy}; Fig. 10). The main difference between $CaFe_2P_2$ and $CaNi_2P_2$ is the position of the Fermi level which lies below the peak corresponding to antibonding Fe–Fe $d_{x^2-y^2}$–$d_{x^2-y^2}$ interactions in the first compound while the additional four electrons per unit cell in the $CaNi_2P_2$ compound are responsible for the Fermi level to be situated above this peak. The important consequences are a weakening of the nearest neighbor Ni–Ni d–d σ bonds compared to the respective Fe–Fe bonds and, as will be discussed later, a reduced ionicity of Ca, and thus of P, in the Ni compound.

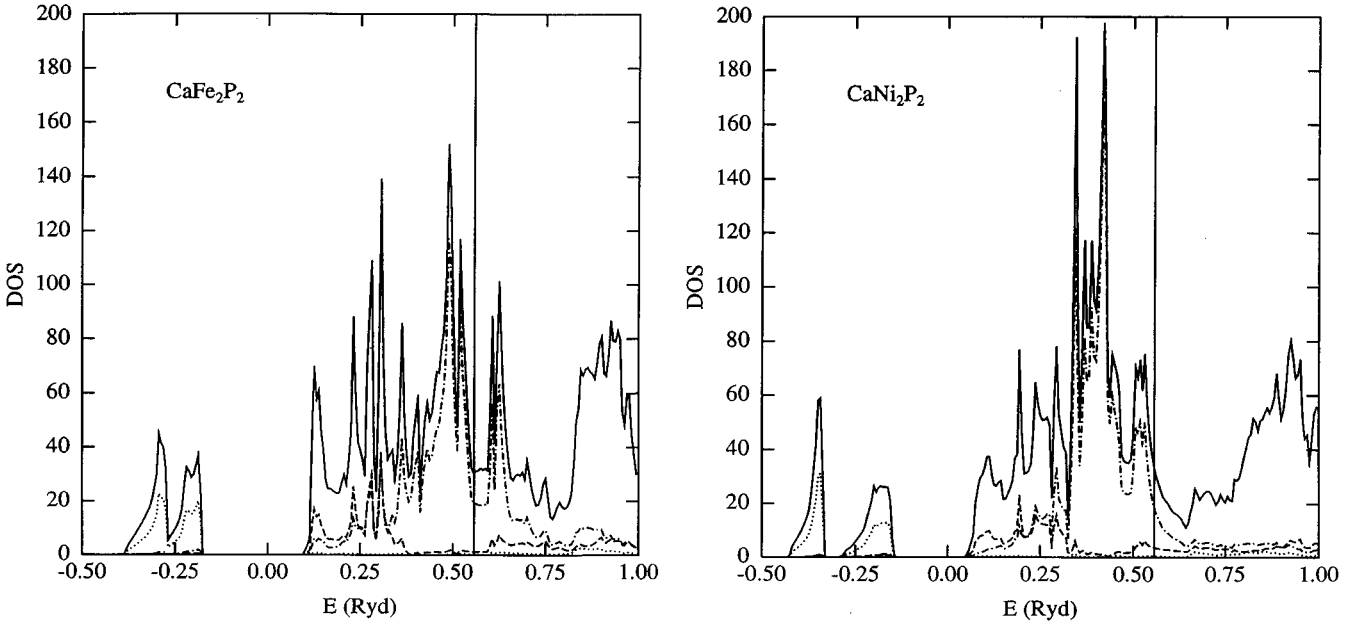

FIG. 3. Total DOS (——), P s (· · · · ·), P p(– – –), and Fe/Ni d(– · – ·) local partial DOS components for $CaFe_2P_2$ (left) and $CaNi_2P_2$ (right) in units of one-electron states per Rydberg and per unit cell.

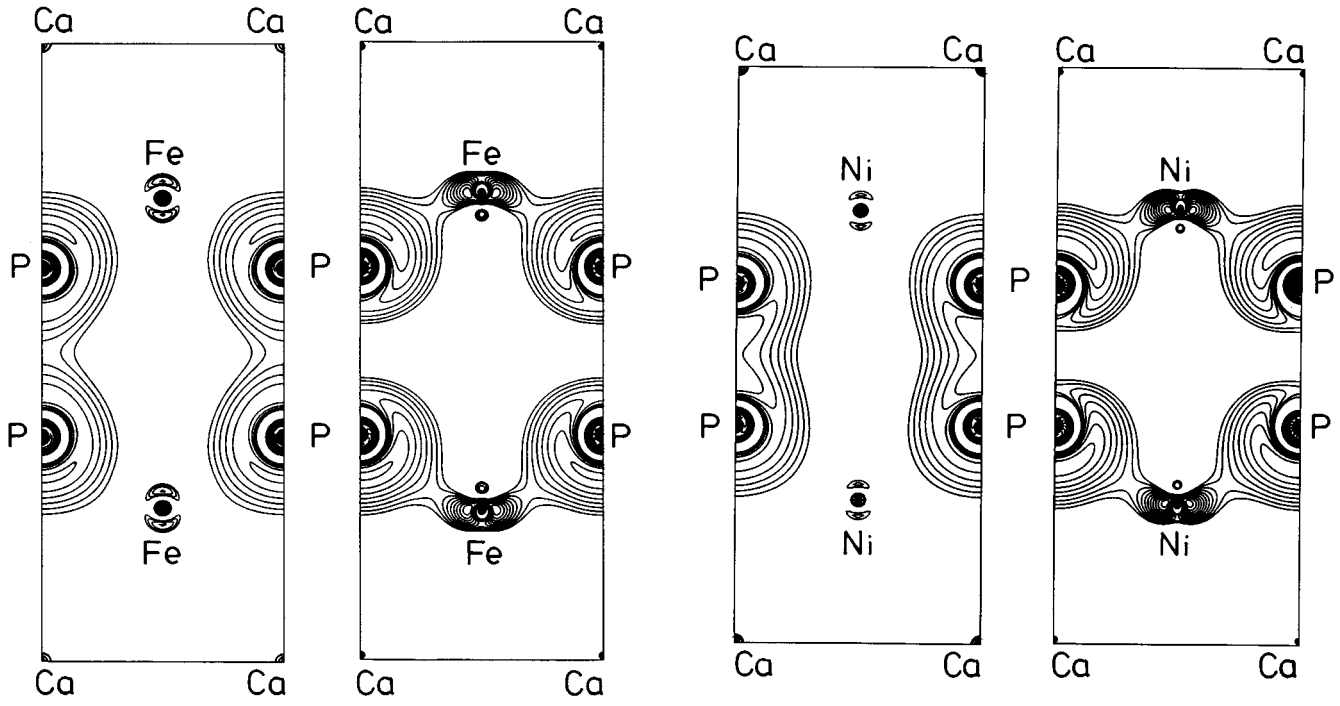

FIG. 4. Electron density plots in the (100) plane for the Γ states at −0.3895 and −0.1783 Ry for $CaFe_2P_2$ (left), and at −0.4307 and −0.1419 Ry for $CaNi_2P_2$ (right). A logarithmic grid of contour lines has been used ($x_i = x_0 2^{i/3}$, $x_0 = 0.02\ e/Å^3$). For a charge analysis of these states see Table 3.

(b) Electron Densities and Chemical Bonding

Figure 11 shows the valence electron densities of $CaFe_2P_2$ and $CaNi_2P_2$ for the (100) plane and for the (001) plane through the Fe/Ni atoms. The plots clearly demonstrate the distinctly stronger P–P bonds in $CaNi_2P_2$. Maxima inside the transition metal spheres are only visible in $CaFe_2P_2$ where they point toward the second nearest neighbor Fe atoms, while a spherical electron density about the Ni atoms is observed which is due to the fully occupied *d* shell in $CaNi_2P_2$. The electron densities between the transition metal atom and P indicate slightly stronger bonds between these atoms in $CaFe_2P_2$, in accordance with the observed bond distances (see Table 3).

TABLE 3
Nearest Neighbors and Shortest Interatomic Distances in $CaFe_2P_2$ and $CaNi_2P_2$ (in a. u.)

$CaFe_2P_2$				$CaNi_2P_2$			
Ca	8	Fe	5.9598	Ca	8	Ni	5.7668
Ca	8	P	5.7525	Ca	8	P	5.6645
Fe	2	Ca	5.9598	Ni	2	Ca	5.7668
Fe	4	Fe	5.1512	Ni	4	Ni	5.2327
Fe	4	P	4.2331	Ni	4	P	4.3326
P	4	Ca	5.7525	P	4	Ca	5.6645
P	4	Fe	4.2331	P	4	Ni	4.3326
P	1	P	5.1210	P	1	P	4.3384

The valence electron density in the (110) plane (Fig. 12, top) shows the covalent bonds between the P atoms and the (relatively small) Ca–P bonding contributions. From this figure the characteristic differences in the bonding properties of the two compounds become obvious, i.e., stronger bonds between nearest neighbor P atoms and weaker bonds between second nearest neighbor P atoms in $CaNi_2P_2$ compared to $CaFe_2P_2$. From the bottom part of Fig. 12 the more pronounced covalent Ca–Ca interactions in the Ni compound can be seen. The spherical electron density between the four Ca atoms originates from the P–P p_z–p_z bonds which are perpendicular to the presented plane and are stronger for $CaNi_2P_2$.

A more detailed analysis can be performed by comparing electron density plots for some selected states for $CaFe_2P_2$ and $CaNi_2P_2$. For these states the *l*-like partial charges within the muffin-tin spheres are given in Table 4. Notice that the percentages not allotted are mainly due to the interstitial region.

Figures 4–6 show the various different P–P bonds which occur in these two compounds, i.e., the P–P *s*–*s* σ and σ^* bonds (Fig. 4), the p_z–p_z σ and σ^* bonds (Fig. 5), and the weaker (p_x, p_y)–(p_x, p_y) bonds between second nearest

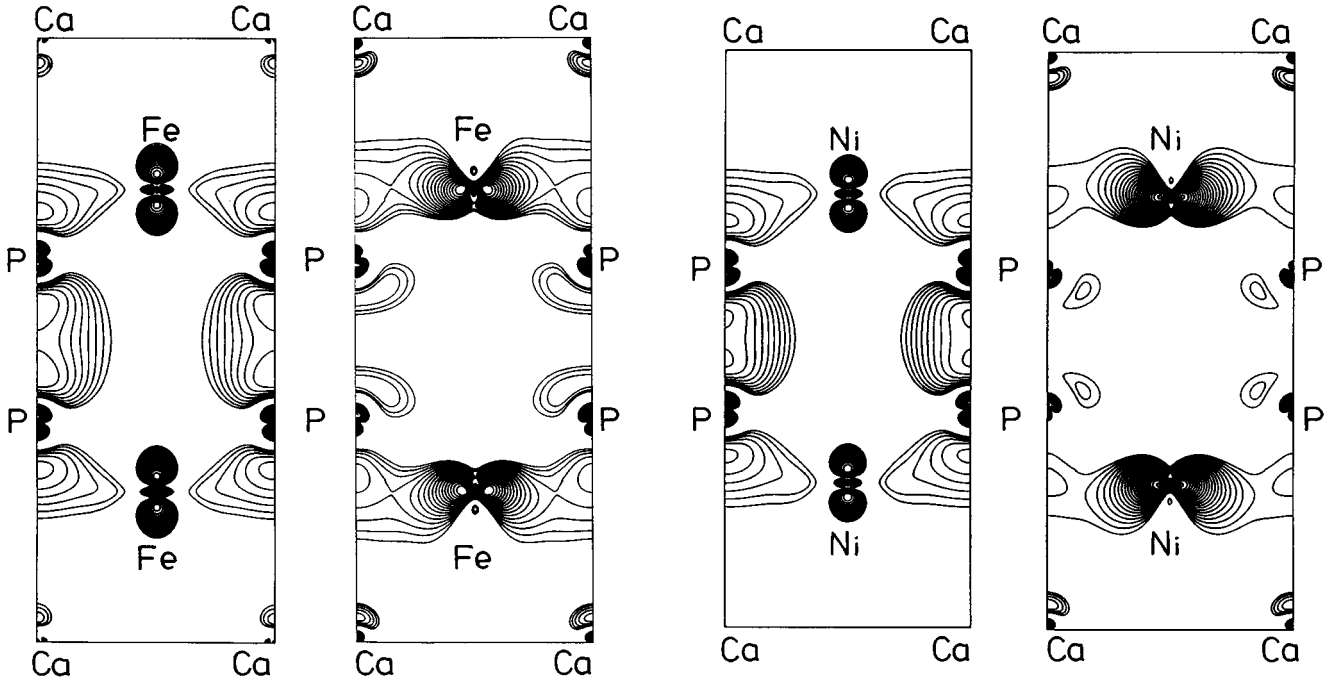

FIG. 5. Electron density plots in the (100) plane for the Γ states at 0.0926 and 0.2958 Ry for $CaFe_2P_2$ (left), and at 0.0420 and 0.3236 Ry for $CaNi_2P_2$ (right). A logarithmic grid of contour lines has been used ($x_i = x_0\, 2^{i/3}$, $x_0 = 0.02\, e/Å^3$). For a charge analysis of these states see Table 3.

P neighbors (Fig. 6). In Fig. 4 the bonding state reflects what can also be deduced from the valence electron densities, namely a distinctly stronger P–P bond for $CaNi_2P_2$ compared to $CaFe_2P_2$. The state which is antibonding with respect to the P–P bond forms Fe–P/Ni–P $d_{xy}(p_z)$–s bonds that are almost equally strong for both compounds. A similar behavior is found for the P–P p_z–p_z bonds (Fig. 5): the P–P bonding state forms Fe–P/Ni–P d_{z^2}–p_z bonds. The antibonding P–P state, however, is involved in Fe–P/Ni–P d_{xy}–p_z bonding interactions which are more pronounced in the iron compound. A striking feature of Figs. 4 and 5 is that the antibonding P–P s–s and p_z–p_z states form considerably stronger Fe/Ni–P bonds than the corresponding bonding P–P states.

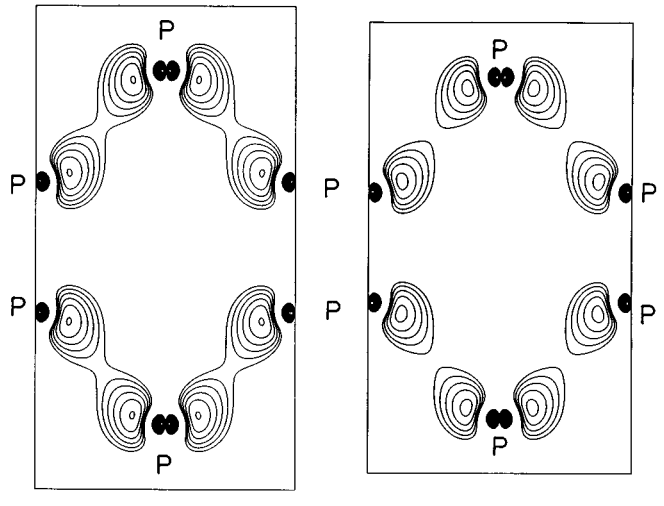

FIG. 6. Electron density plots in the (110) plane for the Γ state at 0.3521 Ry for $CaFe_2P_2$ (left) and at 0.3237 Ry for $CaNi_2P_2$ (right). A logarithmic grid of contour lines has been used ($x_i = x_0\, 2^{i/3}$, $x_0 = 0.02\, e/Å^3$). For a charge analysis of these states see Table 3.

The electron densities for two states typical for Fe–P/Ni–P (d_{xz}, d_{yz})–(p_x, p_y) bonding and antibonding interactions are shown in Fig. 7. For the bonding state one notices an Fe–P bond in $CaFe_2P_2$ stronger than the Ni–P bond in $CaNi_2P_2$ in accordance with the total valence electron densities. In the case of $CaFe_2P_2$ one also notices a weak covalent Ca–Fe bonding contribution for the antibonding state with respect to Fe–P.

The next two figures deal with states forming Fe–Fe/Ni–Ni bonds. Characteristic states for the first and second nearest neighbor interactions are displayed in Figs. 8 and 9. In both figures the Fe–Fe bonds are stronger than the corresponding Ni–Ni bonds. In Fig. 9 the interactions that are σ and σ^* interactions for second nearest neighbors are simultaneously π and π^* interactions for the nearest Fe–Fe/Ni–Ni neighbors. Apart from this it is important to

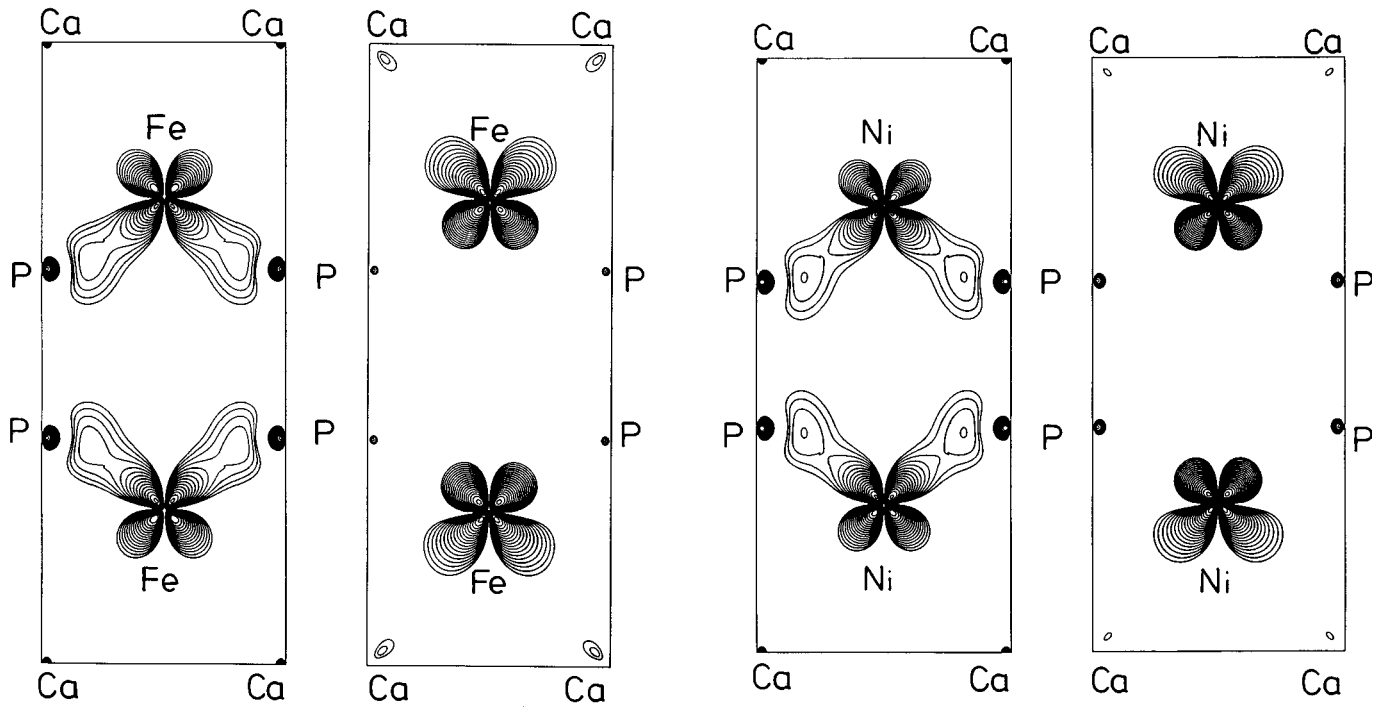

FIG. 7. Electron density plots in the (100) plane for the Γ states at 0.2646 and 0.5354 Ry for $CaFe_2P_2$ (left), and at 0.2413 and 0.4624 Ry for $CaNi_2P_2$ (right). A logarithmic grid of contour lines has been used ($x_i = x_0\, 2^{i/3}$, $x_0 = 0.02\, e/Å^3$). For a charge analysis of these states see Table 3.

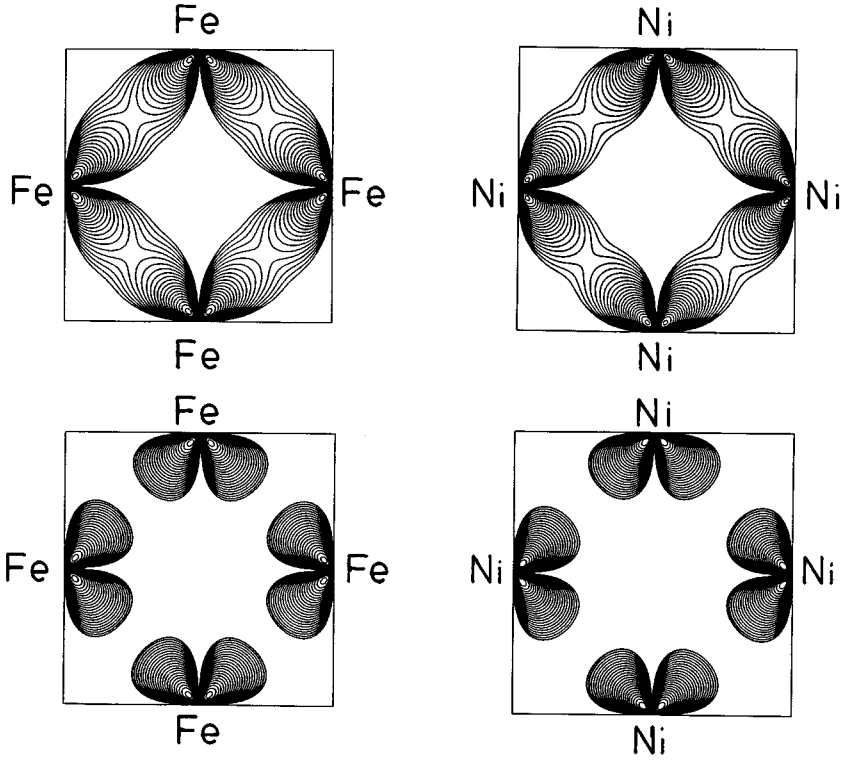

FIG. 8. Electron density plots in the (001) plane for the Γ states at 0.3323 (top left) and 0.5964 Ry (bottom left) for $CaFe_2P_2$, and at 0.3262 (top right) and 0.4968 Ry (bottom right) for $CaNi_2P_2$. A logarithmic grid of contour lines has been used ($x_i = x_0\, 2^{i/3}$, $x_0 = 0.02\, e/Å^3$). For a charge analysis of these states see Table 3.

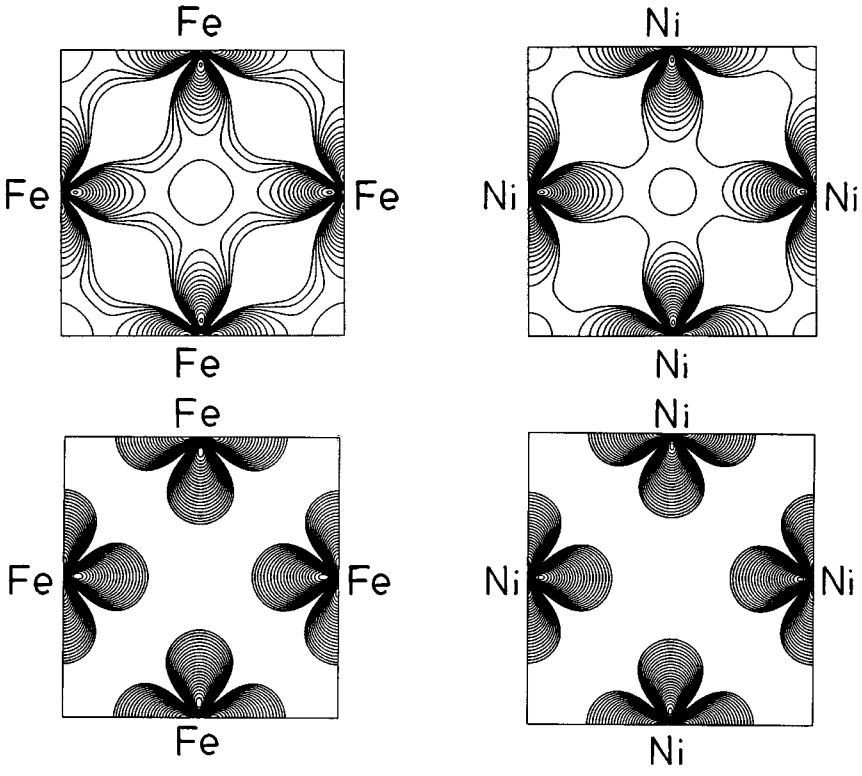

FIG. 9. Electron density plots in the (001) plane for the Γ states at 0.2958 (top left) and 0.5439 Ry (bottom left) for $CaFe_2P_2$, and at 0.3236 (top right) and 0.4500 Ry (bottom right) for $CaNi_2P_2$. A logarithmic grid of contour lines has been used ($x_i = x_0 2^{i/3}$, $x_0 = 0.02\ e/\text{Å}^3$). For a charge analysis of these states see Table 3.

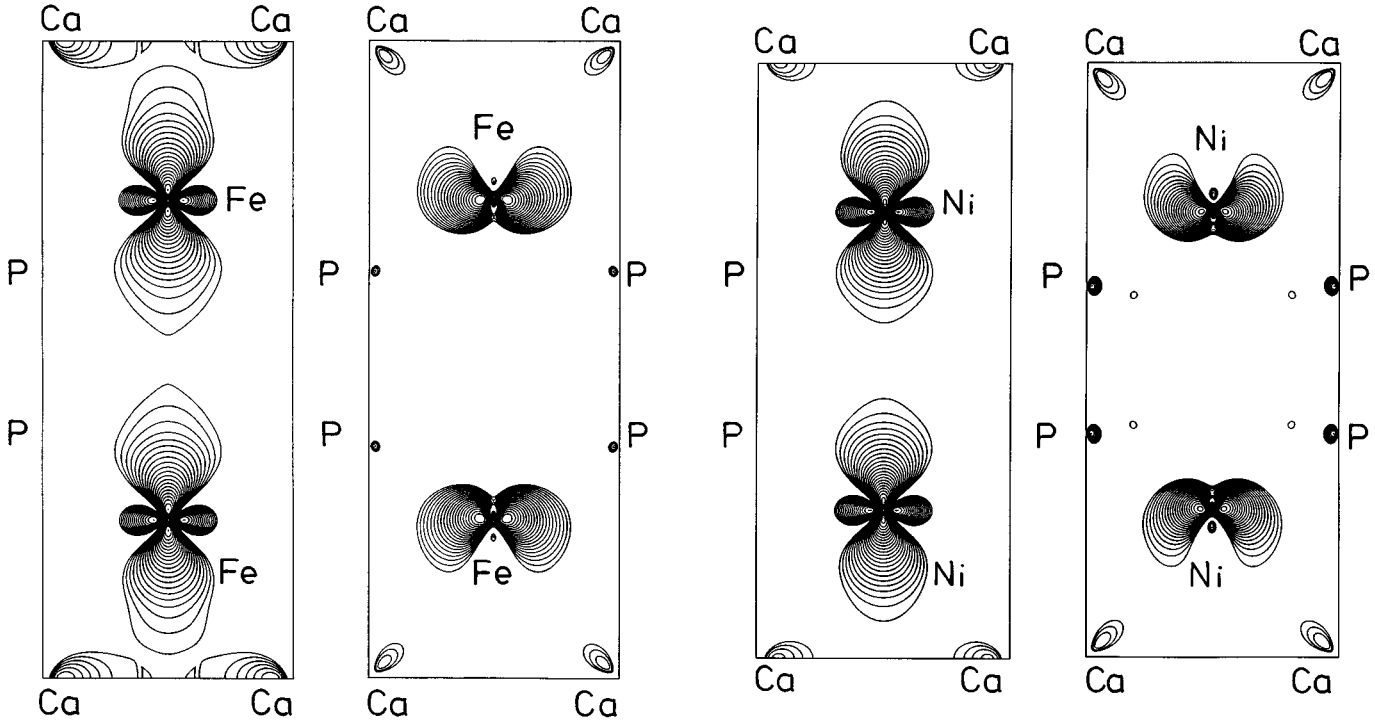

FIG. 10. Electron density plots in the (100) plane for the Z state at 0.4416 and the X state at 0.5053 Ry for $CaFe_2P_2$ (left), and the corresponding states at 0.3793 and 0.4618 Ry for $CaNi_2P_2$ (right). A logarithmic grid of contour lines has been used ($x_i = x_0 2^{i/3}$, $x_0 = 0.02\ e/\text{Å}^3$). For a charge analysis of these states see Table 3.

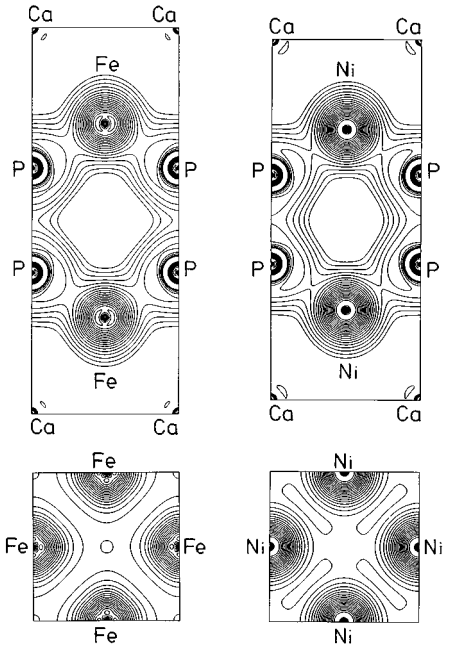

FIG. 11. Valence electron densities for $CaFe_2P_2$ (left) and $CaNi_2P_2$ (right). Top row: (100) planes, bottom row: (001) planes through the Fe/Ni atoms. A logarithmic grid of contour lines has been used ($x_i = x_0\, 2^{i/3}$, $x_0 = 0.2\ e/\text{Å}^3$).

bear in mind that the antibonding state for the nearest neighbor interaction shown in Fig. 8 is unoccupied for $CaFe_2P_2$ while it is below the Fermi level for $CaNi_2P_2$.

Figure 10 is dedicated to the weaker and less important bonding contributions in $CaFe_2P_2$ and $CaNi_2P_2$. For each compound the electron density for a Z state is shown, representing Ca–Ca $d_{x^2-y^2}$–$d_{x^2-y^2}\,\sigma$, Ca–Fe/Ca–Ni $d_{x^2-y^2}$–d_{z^2}, and Fe–Fe/Ni–Ni d_{z^2}–d_{z^2} third nearest neighbor (4.99 Å for $CaFe_2P_2$, 4.68 Å for $CaNi_2P_2$) bonding interactions as well as, for a state of X symmetry, Ca–Fe/Ca–Ni (d_{xz}, d_{yz})–d_{xy} interactions.

CONCLUSIONS

The calculated band structures (Fig. 2) show that both $CaFe_2P_2$ and $CaNi_2P_2$ behave as metals.

For $CaNi_2P_2$ a peak is found in the DOS (Fig. 3) below the Fermi level which corresponds to antibonding Ni–Ni $d_{x^2-y^2}$–$d_{x^2-y^2}\,\sigma^*$ interactions, whereas the respective states for $CaFe_2P_2$ are unoccupied.

From the presented electron density plots (Figs. 4–12) for all valence states as well as for some characteristic single states it can be deduced that (i) the P–P s–s and p–$p\,\sigma$ bonds are stronger for $CaNi_2P_2$ than for $CaFe_2P_2$, (ii) the Fe/Ni–P interactions are slightly stronger in the iron compound, and (iii) the Fe–Fe bonds in $CaFe_2P_2$ are distinctly stronger than the Ni–Ni bonds in $CaNi_2P_2$ mainly due to the occupation of antibonding states. Additional but less pronounced covalent bonding occurs between the Ca atoms within the (001) plane and between Ca and Fe/Ni in both compounds.

The d electron configuration of the transition metal in both phosphides can be deduced fairly accurately. In the nickel compound the d band is almost completely filled (as can be seen from the DOS in Fig. 3 and from the practically perfect spherical symmetry of the valence electron density in the Ni sphere in Fig. 11) which means a d^{10} configuration to a reasonable approximation. In the iron compound about

TABLE 4
Partial Charges (in Percent) for Those States for Which Electron Density Plots Are Presented in This Paper

		$CaFe_2P_2$				$CaNi_2P_2$			
k	l	E (Ry)	Ca	Fe	P	E (Ry)	Ca	Ni	P
Γ	s	−0.3895	3.2	7.2	43.5	−0.4307	3.6	6.1	45.2
Γ	s	−0.1783	0.0	0.0	55.1	−0.1419	0.0	0.0	52.5
	p		0.7	2.2	1.0		0.5	2.3	2.4
	d		0.0	7.9	0.1		0.0	8.4	0.1
Γ	s	0.0926	1.9	5.1	0.6	0.0420	0.2	7.9	0.7
	p		0.0	0.0	26.4		0.0	0.0	30.2
	d		3.4	9.9	0.0		3.4	7.7	0.3
Γ	p	0.2646	1.9	0.4	24.4	0.2413	2.3	0.4	22.1
	d		0.0	40.0	0.0		0.0	44.2	0.0
Γ	s	0.2958	0.0	0.0	2.5	0.3236	0.0	0.0	4.2
	p		4.6	1.5	12.7		4.8	1.9	5.4
	d		0.0	36.5	1.6		0.0	49.6	1.9
Γ	d	0.3323	0.5	74.6	2.0	0.3262	0.6	80.2	1.3
Γ	p	0.3521	0.0	7.3	32.6	0.3237	0.0	6.8	26.3
	d		3.5	14.4	6.7		3.1	24.8	1.0
Γ	p	0.5354	0.0	2.0	1.7	0.4624	0.0	3.5	4.6
	d		6.7	70.9	0.0		6.6	64.5	0.1
Γ	d	0.5439	1.7	86.2	2.1	0.4500	0.2	92.6	1.0
Γ	d	0.5964	0.0	96.1	0.0	0.4968	0.0	96.8	0.0
Z	s	0.4416	0.0	3.5	0.0	0.3793	0.0	3.5	0.0
	d		12.0	48.6	2.6		8.1	60.5	2.0
X	p	0.5053	0.0	1.8	2.3	0.4618	0.0	3.6	8.6
	d		10.6	58.7	1.5		12.6	46.2	0.3

Note. Only lines for significant contributions are given. The energies are given with respect to the average potential in the interstitial region.

TABLE 5
***l*-Like and Total Valence Electron Charges per Atomic Sphere**

	$CaFe_2P_2$			$CaNi_2P_2$		
	Ca	Fe	P	Ca	Ni	P
s	0.180	0.196	1.069	0.186	0.239	1.056
p	0.244	0.219	1.544	0.267	0.235	1.547
d	0.511	5.851	0.135	0.576	7.940	0.124
Total	0.990	6.277	2.762	1.095	8.422	2.739

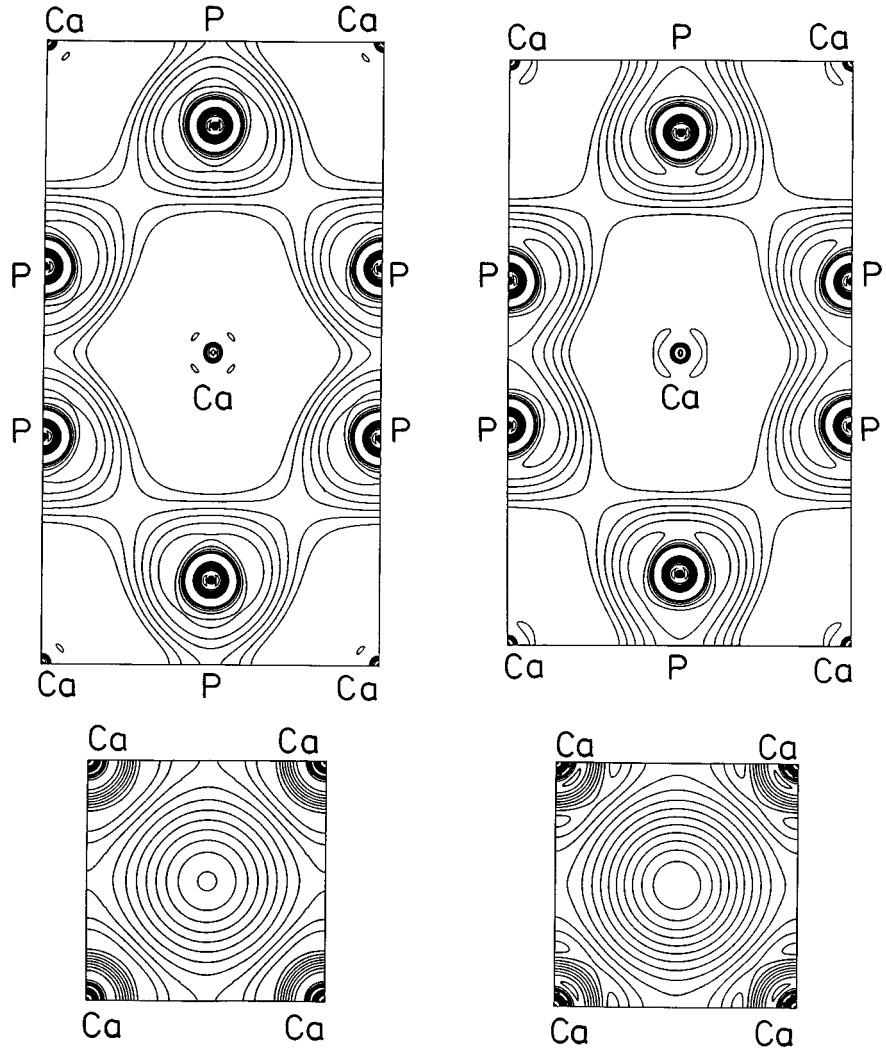

FIG. 12. Valence electron densities for $CaFe_2P_2$ (left) and $CaNi_2P_2$ (right). Top row: (110) planes, bottom row: (001) planes through the Ca atoms. A logarithmic grid of contour lines has been used ($x_i = x_0 2^{i/3}$, $x_0 = 0.2\ e/\text{Å}^3$).

two d electrons less than in the nickel compound are found (see Table 5), leading to an approximate configuration of d^8. These two d electrons correspond to the unoccupied peak in the DOS (Fig. 3) and have predominantly $d_{x^2-y^2}$ symmetry.

The rise of the Fermi level due to the presence of four additional electrons per unit cell in $CaNi_2P_2$ has important consequences for the bonding properties. An analysis of the electronic charge in the Ca spheres shows that 0.10 more electrons are present in $CaNi_2P_2$ compared to $CaFe_2P_2$. An opposite effect is observed for the P spheres (see Table 5). This means that the Ca atoms form stronger covalent Ca–Ca and Ca–P bonds in $CaNi_2P_2$ compared to $CaFe_2P_2$. This can also be deduced from the valence electron density plots for the (001) plane through the Ca atoms (Fig. 12). The higher covalency of the Ca atoms in the Ni compound leads to a stronger covalent interaction, and thus reduced distance, between nearest neighbor P atoms belonging to different Ni_2P_2 layers. We do not find, however, a depletion of filled P–P p_{z^2}–p_{z^2} σ^* orbitals when going from the iron to the nickel compound as has been suggested as a general trend for the transition-metal series by Hoffmann and Zheng (13).

Summarizing, it can be concluded that $CaFe_2P_2$ is slightly more ionic and less covalent than $CaNi_2P_2$. The covalent interactions are stronger *between* the Ni_2P_2 layers than between the Fe_2P_2 layers. This is reflected by the bonds between nearest P–P neighbors as well as by the Ca–Ca and Ca–P interactions. In $CaFe_2P_2$, however, the covalent Fe–Fe bonds *within* the Fe_2P_2 layers are more pronounced than the corresponding bonds in $CaNi_2P_2$.

In a further paper the energetics of these compounds and in particular the dependence of the total energy from the P–P distance will be investigated using the full-potential FLAPW method (18).

ACKNOWLEDGMENTS

We are grateful to the Austrian Fonds zur Förderung der wissenschaftlichen Forschung for financial support (Project P11393).

REFERENCES

1. Z. Ban and M. Sikirica, *Acta. Crystallogr.* **18,** 594–599 (1965).
2. O. S. Zarechnyuk, P. I. Kripyakevich, and E. I. Gladyshevskii, *Kristallografiya* **9,** 835–838 (1964); *Sov. Phys. Crystallogr.* **9,** 706–708 (1965).
3. E. V. Sampathkumaran, G. Wortmann, and G. Kaindl, *J. Magn. Magn. Mater.* **54–57,** 347–348 (1986).
4. W. Jeitschko, R. Glaum, and L. Boonk, *J. Solid State Chem.* **69,** 93–100 (1987).
5. A. Szytula and J. Leciejewicz, *in* "Handbook on the Physics and Chemistry of Rare Earth" (K. A. Gschneidner, Jr. and L. Eyring, Eds.), Vol. 12, p. 133–211. Elsevier, Amsterdam, 1989.
6. M. Reehuis, W. Jeitschko, M. H. Möller, and P. J. Brown, *J. Phys. Chem. Solids* **53,** 687–690 (1992).
7. A. Mewis, *Z. Naturforsch. B* **35,** 141–145 (1980).
8. H. Raffius, E. Mörsen, B. D. Mosel, W. Müller-Warmuth, T. Hilbich, M. Reehuis, T. Vomhof, and W. Jeitschko, *J. Phys. Chem. Solids* **52,** 787–795 (1991).
9. W. Jeitschko and M. Reehuis, *J. Phys. Chem. Solids* **48,** 667–673 (1990).
10. O. K. Andersen, *Phys. Rev. B* **12,** 3060–3083 (1975).
11. D. D. Koelling and G. O. Arbman, *J. Phys. F.: Metal Phys.* **5,** 2041–2054 (1975).
12. E. Wimmer, H. Krakauer, M. Weinert, and A. J. Freeman, *Phys. Rev. B* **24,** 864 (1981); H. J. F. Jansen and A. J. Freeman, *Phys. Rev. B* **30,** 561 (1984).
13. R. Hoffmann and C. Zheng, *J. Phys. Chem.* **89,** 4175–4181 (1985).
14. C. Zheng and R. Hoffmann, *J. Solid State Chem.* **72,** 58–71 (1988).
15. C. Zheng, *J. Am. Chem. Soc.* **115,** 1047–1051 (1993).
16. U. v. Barth and L. Hedin, *J. Phys. C.: Solid State Phys.* **5,** 1629 (1972).
17. O. Jepsen and O. K. Andersen, *Solid State Commun.* **9,** 1763 (1971); G. Lehmann and M. Taut, *Phys. Status Solidi B* **54,** 469 (1972).
18. E. Gustenau, P. Herzig, and A. Neckel, to be published.